Lawrence Berkeley National Laboratory

LBL Publications

Title

Coordination Chemistry as a Universal Strategy for a Controlled Perovskite Crystallization

Permalink

https://escholarship.org/uc/item/41n6d7mc

Journal

Advanced Materials, 35(39)

ISSN

0935-9648

Authors

Zuo, Weiwei

Byranvand, Malekshahi

Kodalle, Tim

et al.

Publication Date

2023-09-01

DOI

10.1002/adma.202302889

Copyright Information

This work is made available under the terms of a Creative Commons Attribution-NonCommercial License, available at https://creativecommons.org/licenses/by-nc/4.0/

Peer reviewed

eScholarship.org Powered by the California Digital Library
University of California

Coordination Chemistry as a Universal Strategy for a Controlled Perovskite Crystallization

Weiwei Zuo,[1] Mahdi Malekshahi Byranvand,[1,2,] Tim Kodalle,[3] Mohammadreza Zohdi,[1] Jaekeun Lim,[1] Brian Carlsen,[4] Theresa Magorian Friedlmeier,[5] Małgorzata Kot,[6] Chittaranjan Das,[1, 2] Jan Ingo Flege,[6] Wansheng Zong,[7] Antonio Abate,[8,9] Carolin M. Sutter-Fella,[3] Meng Li,[10] and Michael Saliba[1, 2,*]*

Weiwei Zuo, Mahdi Malekshahi Byranvand, Mohammadreza Zohdi, Jaekeun Lim, Chittaranjan Das, Michael Saliba
Institute for Photovoltaics (*ipv*), University of Stuttgart, Pfaffenwaldring 47, 70569, Stuttgart, Germany
E-mail: mahdi.malekshahi@ipv.uni-stuttgart.de, michael.saliba@ipv.uni-stuttgart.de

Mahdi Malekshahi Byranvand, Chittaranjan Das, Michael Saliba
Helmholtz Young Investigator Group FRONTRUNNER, IEK5-Photovoltaik, Forschungszentrum Jülich, 52425, Jülich, Germany

Tim Kodalle, Carolin M. Sutter-Fella
Molecular Foundry, Lawrence Berkeley National Laboratory, 1 Cyclotron Road, Berkeley, 94720 California, USA

Brian Carlsen
Laboratory of Photomolecular Science, École Polytechnique Fédérale de Lausanne, 1015 Lausanne, Switzerland

Theresa Magorian Friedlmeier
Zentrum für Sonnenenergie- und Wasserstoff-ForschungBaden-Württemberg (ZSW)70563 Stuttgart, Germany

Małgorzata Kot, Jan Ingo Flege

BTU Cottbus-Senftenberg, Konrad-Zuse-Strasse 1, 03046 Cottbus, Germany

Wansheng Zong
Organisch-Chemisches Institut, Ruprecht-Karls-Universität Heidelberg, Im Neuenheimer Feld 270, 69120 Heidelberg

Antonio Abate
Helmholtz-Zentrum Berlin für Materialien und Energie GmbH, Hahn-Meitner-Platz 1, 14109 Berlin, Germany.
Department of Chemical, Materials and Production Engineering, University of Naples Federico II, pzz.le Vincenzo Tecchio 80, 80125 Naples, Italy.

Meng Li
Key Lab for Special Functional Materials of Ministry of Education, National & Local Joint Engineering Research Center for High-efficiency Display and Lighting Technology, School of Materials Science and Engineering, Collaborative Innovation Center of Nano Functional Materials and Applications, Henan University, Kaifeng 475004, China.

Keywords: coordination chemistry, perovskite crystallization, green solvents

Abstract

The most efficient and stable perovskite solar cells (PSCs) are made from complex mixture of precursors. Typically, to then form a thin film, an extreme oversaturation of the perovskite precursor is initiated to trigger nucleation sites, e.g. by vacuum, an airstream or a so-called antisolvent. Unfortunately, most such oversaturation triggers do not expel the lingering (and highly coordinating) dimethyl sulfoxide (DMSO), which is used as a precursor solvent, from the thin films; this detrimentally affects long-term stability. Here, we introduce (the green) dimethyl sulfide (DMS) as a novel nucleation trigger for perovskite films combining, uniquely, high coordination and high vapor pressure. This gives DMS a universal scope: DMS replaces other solvents by coordinating more strongly and removes itself once the film formation is finished. To demonstrate this novel coordination chemistry approach, we process $MAPbI_3$ PSCs, typically dissolved in hard-to-remove (and green) DMSO achieving 21.6% efficiency, among the highest reported efficiencies for this system. To confirm the universality of our strategy, we tested DMS for $FAPbI_3$ as another composition, which showed higher efficiency of 23.5% compared to 20.9% for fabricated device with Chlorobenzene. This work provides a universal strategy to control perovskite crystallization using coordination chemistry heralding the revival of perovskite compositions with pure DMSO.

1. Introduction

The power conversion efficiency (PCE) of perovskite solar cells (PSCs) with an ABX_3 structure - where A= Cs^+, methylammonium (MA^+), formamidinium (FA^+); B= Sn^{2+} or Pb^{2+}; X= Cl^-, Br^- or I^- - have sky-rocketed from 3.8%[1] in 2009 to now 25.7%[2]. To achieve higher thermal, moisture, and phase stabilities, we and others have designed various compositions based primarily on mixtures of $FAPbI_3$ with additives such as K^+, Rb^+, Br^-, Cl^-, SCN^-, and more.[3–6] Essentially, the purpose of this multicomponent engineering approach is to stabilize the photoactive "black phase" of $FAPbI_3$ at room temperature. This complexity, however, imposes challenges during film processing.[7]

At the same tune, solvent engineering is equally important to manipulate the crystallization of perovskite films.[8] Currently, an antisolvent is used to supersaturate the perovskite precursor during the spin coating, e.g. chlorobenzene (CB), which is orthogonal on mixture N,N-Dimethylformamide (DMF) and dimethyl sulfoxide (DMSO). Typically, a mixture of DMSO and DMF is used to dissolve multicomponent perovskites. The usage of the antisolvent is followed by nucleation during the subsequent annealing step.[9–14]

Currently, the antisolvent is used naively since there is no or hard-to-predict coordination with the perovskite precursor components depending also on the exact composition used. For example, the all-inorganic $CsPbI_3$ coordinates while hybrid perovskites often do not.[15] Thus, the strongly coordinating DMSO often stays behind in the thin film.

Here, we demonstrate that coordination chemistry with respect to functional group and vapor pressure of solvents. This novel coordination chemistry is enabled by new sulfide-based green solvents such as dimethyl sulfide (DMS), which combines the highest yet reported donicity with among the highest vapor pressures reported in literature. In addition, among the ether-type solvents, DMS is the one that is common in nature. Some ether solvents, such as tetrahydrofuran (THF)[16] and diethyl ether (DE)[17], are also frequently used in the study of perovskite, while we use DMS for the first time as an anti-solvent, and compared diethyl sulfide (DES) and dipropyl sulfide (DPS) with different boiling points based on different carbon branched chain lengths of sulfur atoms to optimize perovskite crystallization. This opens a new door for perovskite research towards a controlled crystallization already at the early film formation stages.

2. Results and Discussion

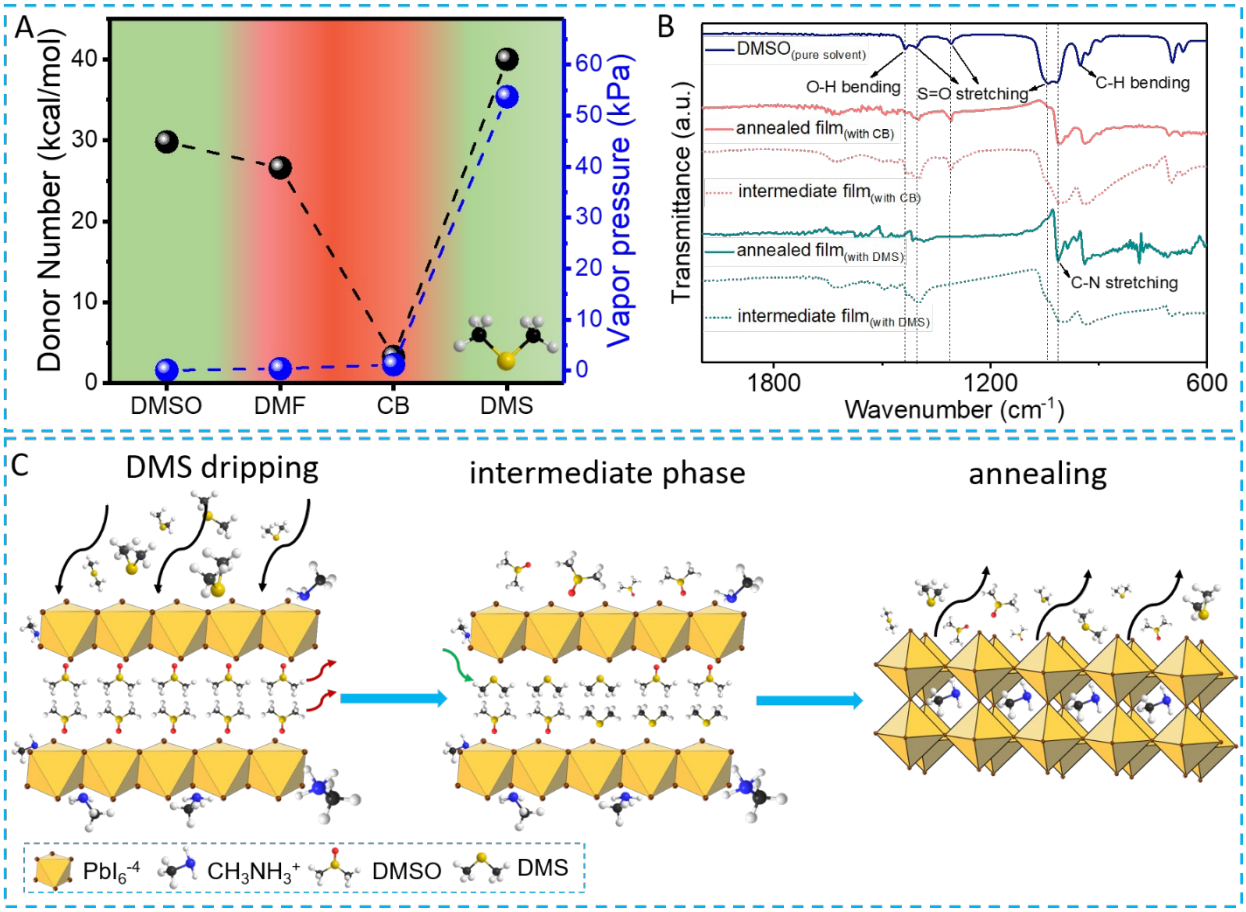

Figure 1 The mechanism of $MAPbI_3$ crystallization by assisting the solvent extraction role of DMS. (**A**) Gutmann donor numbers (D_N) and vapor pressure (at 20°C) of different solvents including DMSO, DMF, CB and DMS. (**B**) The Fourier-transform infrared spectroscopy (FTIR) spectra of pure DMSO, as well as of perovskite films deposited by CB and DMS before (intermediate phase) and after annealing. (**C**) Schematic illustration of the proposed mechanism of DMS for perovskite crystallization.

The Gutmann D_N is a measure of the ability of a solvent to solvate cations and to react with Lewis acids based on coordination chemistry theory.[18,19] **Figure 1A** shows the Gutmann D_N and vapor pressure of DMSO, DMF, CB and DMS as the involved solvents in perovskite films fabrication (all the detailed parameters including D_N, dielectric constant, dipole moment and vapor pressure for all solvents are shown in **Table S1**). Generally, solvents with high D_N coordinate strongly with the Pb^{2+} cations. Therefore, varying the concentration of high-D_N additives in precursor solutions tunes the Pb-solvent interactions.[20,21] Among the typical solvents for perovskite processing, DMS shows the highest D_N and higher vapor pressure.

At the same time, **Figure 1A** also shows that DMSO has a relatively high donor number and a low vapor pressure leading to significant challenges in extracting DMSO from the formed film. Current extraction solvents include CB, which has a low donor number and therefore does not coordinate with DMSO.

To highlight this point, we focus on $MAPbI_3$ in the following since it dissolved in pure DMSO unlike multicomponent perovskites that also use the more volatile DMF as the majority solvent for the precursor preparation. Moreover, the archetypical $MAPbI_3$ has advantages over multicomponent perovskites, such as a stable black phase at room temperature, less risk for phase segregation (only three components are needed), and an almost ideal bandgap at 1.58 eV.[6,7,22–27] While MA's volatility remains a challenge, reports show that appropriate encapsulation is a possible remedy.[28,29]

One challenge with for $MAPbI_3$ films is the instability against temperatures over 100 °C.[30] Thus, using DMSO (high coordination and a boiling point of 189°C) with a very low vapor pressure nucleation trigger, such as CB, leads to a conflict between the perovskite degradation and the required temperature to degas the DMSO during the perovskite annealing (see **Figure 1A**).

To explore the performing mechanism of the solvents during the perovskite crystallization, we conduct Fourier-transform infrared spectroscopy (FTIR) for analyzing the intermediate phases and perovskite films (**Figure 1B**). The FTIR spectrum of pure DMSO is measured as the reference. The pure DMSO shows the S=O stretching peaks at 1400 cm^{-1},1309 cm^{-1}, and 1043 cm^{-1}, respectively. In the spectra of the perovskite intermediate phase obtained using the antisolvent of CB and DMS, the S=O stretching peak at 1043 cm^{-1} is covered by the stretching peak signal of C-N at 1010 cm^{-1}, which then appears as a companion peak in the spectra, and in

the annealed perovskite phase, this stretching peak disappears. The S=O stretching peak at 1400 cm^{-1} disappears only in the spectra of the perovskite phase with DMS as the antisolvent, however, the stretching peak of S=O at 1309 cm^{-1} disappears in the spectra of the perovskite intermediate phase and the annealed black phase when DMS is used as the antisolvent. This suggests that due to the high D_N and the mutual miscibility with DMSO,[31] DMS extract DMSO very efficiently and replaces its position in the MAI-PbI_2-DMSO adduct at the intermediate phase by coordinating its sulfur functional group to the Pb^{2+} cations. Afterwards, DMS can leave the intermediate phase during the annealing process due to its high vapor pressure, leading to uniform nucleation and efficient crystallization. Based on these observations, we schematically illustrate the possible mechanism of DMS as a strong coordination solvent during the perovskite crystallization in **Figure 1C**. In addition, we investigated the initial adsorption of molecular DMS and DMSO using density functional theory (DFT) to understand the interactions between DMS or DMSO and PbI2 (0 0 1) surfaces. Our results show that DMS forms intermediates more readily with PbI_2 than with DMSO (See **Figure S1**, **Table S1** and **Supplementary Note 1**).

To get a more detailed understanding of the perovskite crystallization, we provide in-situ film characterization. **Figure 2** shows the evolution of the photoluminescence (PL) measured in-situ during spin-coating and annealing at 100°C using CB and DMS, respectively. **Figure S2** shows the same evolution for deposited perovskite films by all four solvents. To elucidate the formation dynamics on a structural level, we show in-situ grazing incidence wide-angle X-ray scattering (GIWAXS) patterns of the CB sample in **Figure S3A**. Due to the very low viscosity of DMS, we could not measure in-situ GIWAXS on that corresponding sample. Instead, **Figure S3B** shows the GIWAXS evolution in the case of DES. Combining the PL and the GIWAXS data, we divide the film formation into three growth stages that will be discussed in the following. Comparing the PL-data of all five cases suggests that the perovskite growth follows similar dynamics via these three stages for all solvents.

In Stage I, after the initial solution ejection during the first ~5 seconds of the spin-coating process, there is a weak PL signal emerging centered around 1.58 eV. This signal is also present in the case of DMS but not visible in **Figure 2B** due to the different intensity-scaling of both panels (see color bars on the right side of **Figure 2**) – a differently scaled version of the same plot showing the existence of the weak PL-signal at 1.58 eV is shown in **Figure S4**. GIWAXS during

the first stage only shows peaks associated with the ITO substrates which cannot explain the PL emission (see **Figure S3**). Interestingly, the PL emission peak position coincides with the bandgap of $MAPbI_3$ but $MAPbI_3$ crystallization or formation is not expected and has not been reported before at this early stage and room temperature. Instead, during spin coating, before dripping the solvent, and depending on the exact precursor composition and solvent choice, solvate phases may form quickly.[32] We have shown before, that small volume inclusions of the perovskite phase may not show up in the diffraction pattern but PL is very sensitive to these bright emitting phases.[33] Other in-situ PL studies during perovskite formation found blue-shifted PL emission at the early crystallization stages explained by excitonic confinement in low dimensional perovskite structures.[34] Here, we can only speculate that the weak PL signal in Stage I may be attributed to an amorphous or intermediate, $MAPbI_3$-containing phase.

Upon the solvent drop, the beginning of Stage II, the initial PL-signal vanishes, and distinctive diffraction peaks appear (e.g. at 0.46 $Å^{-1}$, 0.51 $Å^{-1}$, and 0.65 $Å^{-1}$) that can be attributed to the orthogonal crystalline solvent-complex, $Pb_3I_8.2(CH_3)_2SO.2CH_3NH_3$ ($MAPbI_3$·DMSO solvent complex).[42-44] In addition, dropping DMS or CB induces the occurrence of a very intense PL-peak centered at 1.64 and 1.7 eV, respectively, but is not present in the other cases at room temperature. Two possible explanations are considered to explain the PL emission energy higher than the bandgap energy. Dripping of DMS or CB likely leads to an exchange mechanism of DMS or CB with DMSO leading to the formation of a luminescent intermediate phase containing 2D-layered nanosheets or other low dimensional perovskite clusters.[34] In the case of CB and in analogy to a previous report,[33] we interpret the short PL 'flash' in the case of CB as immediate $MAPbI_3$ nanocrystal formation. The PL is blue-shifted compared to the bulk bandgap due to quantum confinement effects. The emergence of PL in the cases of DMS and CB but not for DPS and DES possibly indicates a different interaction with DMSO. For DMS and CB, DMSO is likely removed efficiently and locally during the dripping event while it is not as efficiently extracted with DPS and DES. In the case of CB, the quantum-confined perovskite nuclei formation appears metastable at this stage as large amounts of DMSO are still present in the wet film, hence the PL signal disappears very quickly. As the signal remains constant in the case of DMS, it appears that DMS is more efficiently extracting the DMSO, creating more stable nuclei. In addition, the short-lived PL signal appearing right after CB dripping is more blue-shifted than

the PL peak appearing after DMS dripping which indicates that nuclei are smaller in the case of CB.[35]

During annealing, i.e., in Stage III, the PL-emission of the DMS sample slightly redshifts before the appearance of the $MAPbI_3$-related PL-peak centered around 1.61 eV (see **Figure 2**). The PL intensity drop and re-appearance of the $MAPbI_3$-related PL in the DMS case is likely caused by a second nucleation and growth event upon dissociation of the intermediate phase when reaching the final annealing temperature. With increasing annealing duration, this signal fades due to temperature-induced PL-quenching[36] as well as degradation due to the constant laser-illumination. These dynamics are in good agreement with the GIWAXS data, which shows that the intermediate phase (in all investigated cases) undergoes thermal dissociation and subsequent solvent evaporation leading to the growth of $MAPbI_3$ and PbI_2 crystals (see **Figures S3**).

Judging by the in-situ PL and GIWAXS data, the choice of the solvent and consequently the solvent-solvent interaction as well as the subsequent coordination chemistry do affect the formation dynamics of the final $MAPbI_3$ crystals during annealing. However, there are indications that DMS dripping is the most efficient in extracting DMSO, leads to larger initial nuclei, and a faster and more defined $MAPbI_3$ absorbance edge as measured by in-situ transmission (see highlighted area in **Figure S5**), and a significantly more intense PL-signal, indicating higher crystal quality.

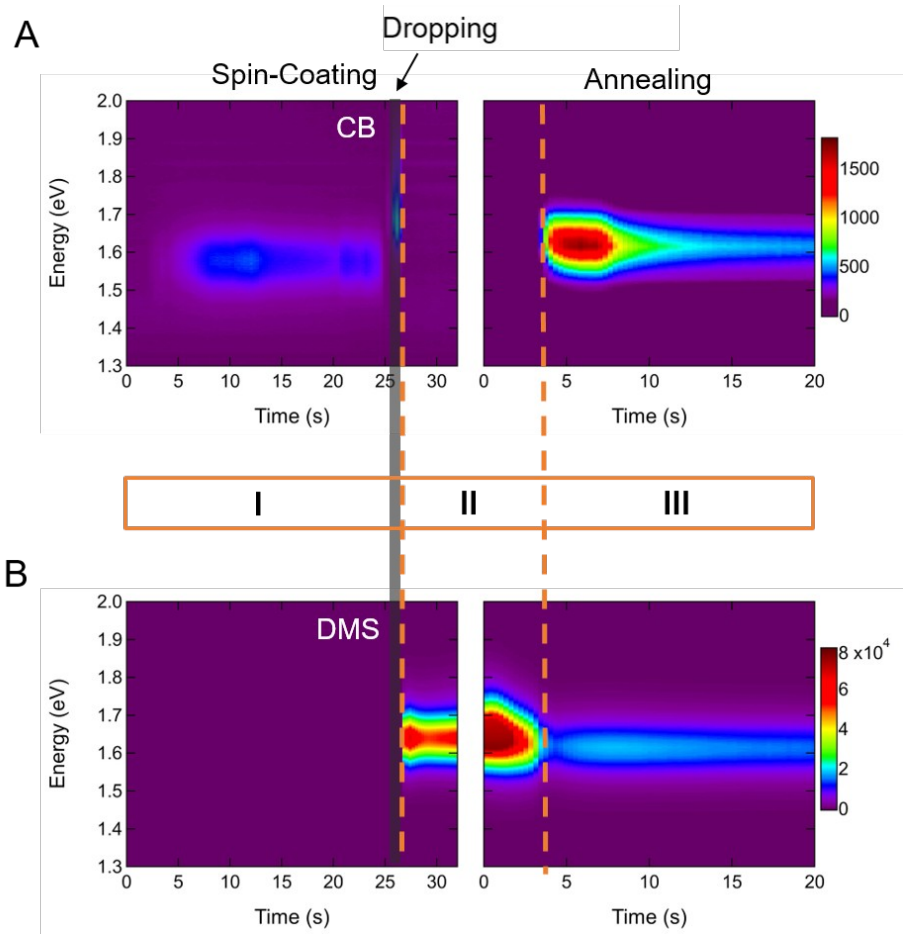

Figure 2 In-situ characterization of perovskite films. The evolution of the photoluminescence signal during spin-coating (left column) and annealing (right column) of a $MAPbI_3$ sample deposited by assisting (**A**) CB and (**B**) DMS. (The black arrow indicates the drop time point of the solvent).

In **Figure 3**, we show the chemical structures and safety information of CB and DMS. CB is a halogenated solvent with flammable, skin/eye irritation and highly toxic properties, which is detrimental to human health and the environment.[37] On the other hand, DMS raises fewer safety concerns and has flammability tendency that can be handled with appropriate precautions. DMS is even used as a food additive at low concentrations.[38,39] A high-resolution scanning electron microscope (SEM) and X-Ray diffraction (XRD) are used to characterize the morphology and crystallinity of the deposited perovskite films. Both cases provide fully formed perovskite films with almost identical thicknesses; while the film deposited without solvent extraction shows a nonuniform coverage with elongated needle-shaped regions (see **Figure S6**).

Previous research explored diethyl ether (DE),[40,41] and ethyl acetate (EA) as green solvents with various polarities and functional groups.[42] The authors show that, due to the higher vapor pressure of DE at 58.9 kPa and EA at 9.69 kPa compared to CB at 1.17 kPa at 20 ºC, the resulting perovskite films exhibit various nonuniformities.[13,41,43] Interestingly, when we deposit perovskite film by DMS coordination solvent with an almost similar vapor pressure to DE (58.9 kPa to 53.7 kPa, respectively) (see **Table S2**), it still results in a compact and homogeneous morphology comparable to CB and other sulfide-based solvents (**Figure S7**). This occurs because the functional group of the solvents appear to play an important role in improved perovskite crystallization[44]

Almost all the sulfide-based solvents have the same functional group, i.e., sulfur, and result in reasonable perovskite films (**Figure S8** and **Table S3**). The perovskite film deposited by DMS presents smaller grain sizes compared to CB, but with much better monodispersity (**Figure 3**). It has been demonstrated that the morphology and grain size of perovskite films also depends on the precursor solvents extraction, the solvents vapor pressures,[17] and processing temperature.[45] As shown in **Figure S9**, the vapor pressure of sulfide-based solvents decreases gradually by decreasing the alkyl chain from DPS to DMS, leading to different evaporation rates during the annealing step, which could be the reason for the different resulting grain sizes. In **Supplementary Note 2**, we provide a more detailed rationale for the solvent selection and proceed for reasons of conciseness with a mechanism discussion next.

The XRD pattern reveals a pronounced PbI_2 peak at 12.7° for CB, indicating incomplete perovskite crystallization (the PbI_2 peak is assigned with a star in **Figure 3**). On the other hand, this peak is absent for DMS, indicating a completed reaction of PbI_2 with the organic cation in the presence of DMS. However, the PbI_2 peak is still present for DES and DPS with lower intensity than the CB case (**Figure S7**).

The surface elemental analysis and PL spectroscopy of fabricated $MAPbI_3$ films demonstrate significant film quality improvement by the action of the DMS coordination solvent (see **Supplementary Note 2**). The X-ray photoelectron spectroscopy (XPS) data show that the amount of Pb^0 is minimized in the DMS film, indicating negligible surface recombination compared to other cases (**Figures S10A** and **B**). The PL data also present the lowest defect density among all the films for the perovskite film fabricated by DMS (**Figures S10C and D**).

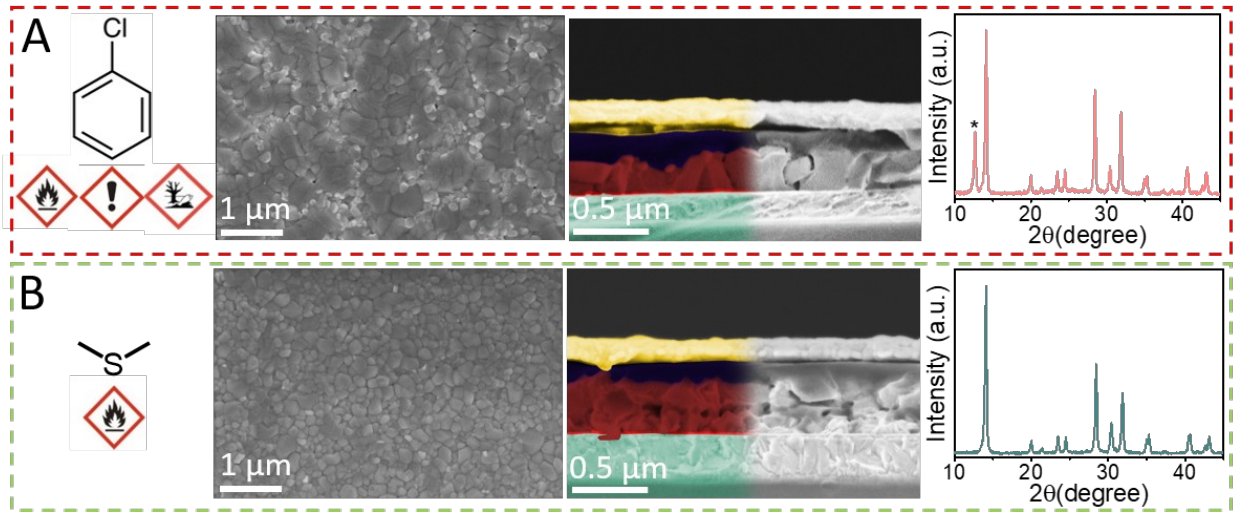

Figure 3. The morphology and crystallinity of $MAPbI_3$ films. Chemical structures and safety pictograms of (**A**) CB and (**B**) DMS. While DMS is only flammable, CB poses further health and environmental hazards. Top-view and cross-sectional SEM images, and the XRD pattern of the corresponding perovskite films.

Finally, we fabricate PSCs in a typical stack of ITO/SnO_2/perovskite/ 2,2′,7,7′-Tetrakis(*N*,*N*-di-*p*-methoxyphenylamine)-9,9′-spirobifluorene (Spiro-OMeTAD)/gold (see **Figure 4A** and fabrication details can be found in the SI). Previously, we used anisole as a green solvent for Spiro-OMeTAD instead of CB.[46] By avoiding DMF, we can process our devices with a fully green solvent system using water [47], DMSO[48], and anisole[46,49] for SnO_2, perovskite precursors, Spiro-OMeTAD, and using DMS for DMSO extraction from the perovskite precursor (see the non-green in **Figure S13** and fully green processing paths in **Figure 4A**).

The statistical photovoltaic parameters, including short-circuit current density (J_{SC}), open-circuit voltage (V_{OC}), fill factor (*FF*), and PCE for 18 devices, measured in reverse scan direction for each antisolvent are seen in **Figure 4B**. The PSCs fabricated by CB present lower photovoltaic parameters than the DMS devices, possibly due to the lower perovskite film quality. Especially V_{OC} and *FF* are significantly increased in the case of DMS, achieving the higher PCEs with high reproducibility. The PSCs fabricated with the other solvents, i.e., DPS, DES, presented reduced photovoltaic performance compared to DMS (see **Figure S14**). In a similar trend, the PSCs using DMS showed negligible hysteresis (**Figure S15**) indicating the dependence of device performance on film quality.[50]

Figure 4B and **Table 1** compare the champion current-voltage (*J–V*) characteristics of PSCs fabricated using CB and DMS. A substantial performance improvement from 19.1% for CB to 21.6% for DMS is observed, mainly due to improved V_{OC} from 1.09 V to 1.16 V and *FF* from 0.76 to 0.81. This PCE of 21.6% is the highest reported value for fully green solvent-processed n-i-p $MAPbI_3$ PSCs (See **Table S4** and **Supplementary Note 3**).

The improved V_{OC} and *FF* of PSCs fabricated by DMS are attributed to the efficient crystallization and defect passivation of the perovskite films. To prove this concept, the ideality factor is determined by measuring the V_{OC} dependence on the light intensity (see characterization methods in the SI). As shown in **Figure S17,** the value of the ideality factor decreases significantly from 1.93 for the devices fabricated by CB to 1.27 for the DMS ones. This result is an indication of reduced surface defects at the perovskite/HTL interface. Additionally, we measure the stabilized power output (SPO) at a fixed maximum power point voltage over time to better understand our photovoltaic observations (**Figure 4B** inset). The PSC fabricated by DMS presents an excellent stabilized PCE of ~20.7% for 180 s, which is very close to the original PCE from the *J–V* curve. In contrast, in the case of CB, SPO decreases over time (stabilized PCE of ~16.7%), which confirms the lower quality of perovskite film causing the high *J–V* hysteresis. Moreover, the PSC fabricated by DMS shows a lower dark current than the CB sample, suggesting a lower dark leakage current due to improved charge transport and decreased recombination loss in the device (See **Figure S18**). The *J-V* curves of the champion cells for all samples are shown in **Figure S19**, and detailed performance parameters are shown in **Table S5**.

As shown in **Figure S20**, the integrated current densities of ~22.3 mA/cm^2 and ~22.3 mA/cm^2 calculated from the external quantum efficiency (*EQE*) spectra of CB and DMS champion devices agree with the current densities of the *J-V* measurement. We also performed a 16-days performance data tracking measurement on 9 devices, and the results showed that the DMS-based solar cells were more stable, which might be due to the passivated defects in the corresponding perovskite films. In contrast, the variance of the performance parameters of the CB solar cells shown in the box charts is bigger. (see **Figure S21** and **Figure S22**).

To prove the universality of our strategy, we fabricated $FAPbI_3$ perovskite solar cells by means of CB and DMS. As shown in **Figure 4c**, similar to $MAPbI_3$ composition, the mean values of V_{oc} and FF for fabricated $FAPbI_3$ solar cells with DMS is significantly increased compared to CB

counterpart. These data demonstrate that even though the fabrication strategies (excluding the antisolvent process) for $FAPbI_3$ and $MAPbI_3$ cells differ, the films fabricated using DMS as an antisolvent show same improvements in device performance when compared to the control group. Moreover, as shown in **Table 1**, the $FAPbI_3$ champion device with DMS showed a high efficiency of 23.5% with excellent FF of 0.84, while the fabricated solar cell with CB showed only 20.9% PCE with 0.78 FF.

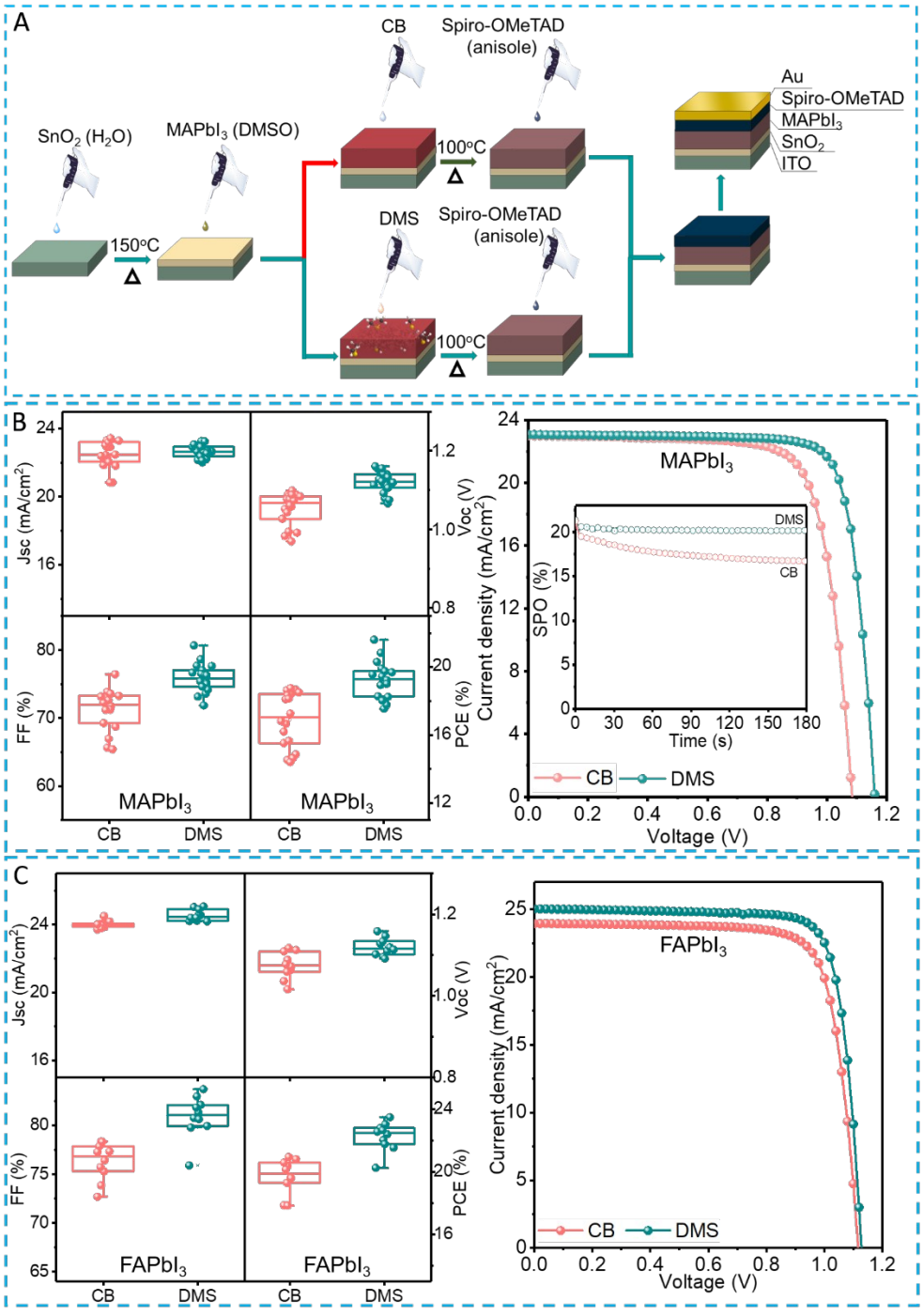

Figure 4 The fabrication process and characterization of PSCs. (**A**) Schematic illustrations of PSCs processing by the fully green and non-green solvents. (**B**) Statistical photovoltaic parameters and champion *J-V* curves of fabricated PSCs of $MAPbI_3$ by CB and DMS (the inset shows the stabilized power output (SPO) at the maximum power point voltage for 180 s). (**C**) Performance Comparison of $FAPbI_3$-based Solar Cells Using DMS and CB as Antisolvents, and Comparison of J-V Curves for Champion Cells.

Table 1 Summary of the photovoltaic parameters obtained from the champion devices for $MAPbI_3$ and $FAPbI_3$ fabricated by CB and DMS. Measurements were performed under AM 1.5 solar illumination.[a]

Composition		V_{OC} (V)	J_{SC} (mA/cm2)	FF	PCE (%)
$MAPbI_3$	CB	1.09	23.0	0.76	19.1
	DMS	1.16	23.0	0.81	21.6
$FAPbI_3$	CB	1.12	23.9	0.78	20.9
	DMS	1.12	25.1	0.84	23.5

[a)] Cell size: 0.16 cm^2. A shadow mask was used to define the active area.

3. Conclusion

Currently, DMF-rich solvent systems are used to dissolve the precursor components of practically all high-performance perovskite solar cells. Unfortunately, DMF hydrolyses and is therefore a long-term risk to stability. One pathway to avoid DMF is the usage of pure DMSO, but this is not an option for the state-of-the-art multicomponent perovskites. Interestingly, the now almost obsolete $MAPbI_3$ perovskite requires pure DMSO but could never reach performances >21% due to the challenging extraction of the DMSO molecules which form their complexes with Pb^{2+}.

Many other reports have introduced "better" antisolvents than CB based on the rationale of supersaturating the perovskite precursor. Instead, here we introduce a novel (and green) solvent, DMS, based on the rationale of strong coordination chemistry for extracting the DMSO from the perovskite precursor efficiently and promote very controllable crystallization. The results show that DMS assists to form the intermediate phase in a short time due to its high Gutmann donor number and mutual solubility with DMSO. This leads to a higher quality perovskite layer than the other similar solvents due its high vapor pressure so that the annealing temperature is well

below the degradation temperature of perovskite. Consequently, in line with industry needs, we show that our novel solvent system can be used as the basis to process all layers, including electron-transporting (ETL), perovskite, and hole-transporting layer (HTL), with green solvents. The fully green-solvent-processed $MAPbI_3$ PSC delivered a world record efficiency of 21.6%. We also used DMS as an antisolvent to fabricate $FAPbI_3$ films. The devices fabricated using DMS as an antisolvent achieved an efficiency of 23.5%, demonstrating superior performance compared to the control devices.

4. Experimental Section

Materials: The chemicals and solvents were obtained commercially and used without further purification. SnO_2 colloid precursor (15% in H_2O colloidal dispersion) was purchased from Alfa Aesar. The organic cation halide salts for perovskite methylammonium iodide (MAI) were purchased from Greatcell Solar Materials. PbI_2 was purchased from TCI. Spiro-OMeTAD (99.5%), 4-Tert-butyl pyridine (99.9%), lithium bis(trifluoromethylsulphonyl) imide (99.95%), and FK209 Co(III) TFSI salt (98%) were purchased from Advanced Election Technology CO,.Ltd, TCI, Sigma-Aldrich, and Dyesol, respectively. All solvents, including Dimethyl sulfoxide (DMSO), chlorobenzene (CB), dimethyl sulfide (DMS), diethyl sulfide (DES), and dipropyl sulfide (DPS), Anisol (ANS), and acetonitrile (ACN) were purchased from Sigma-Aldrich.

Device Fabrication: For $MAPbI_3$, Patterned ITO substrates (7 Ω/sq, AGC) were ultrasonically cleaned with 2% Hellmanex water solution, deionized water, acetone, and IPA. Before use, the as-cleaned substrates were further cleaned with UV ozone treatment for 15 min. Then the SnO_2 solution (2.67%, diluted by water) was spin-coated onto the substrates at 3000 rpm for 25 s and annealed on a hot plate at 150 °C for 30 min under an ambient atmosphere. After cooling down to room temperature, the substrates were treated with UV ozone for 20 min. The perovskite precursor solution was prepared with 1.3M $MAPbI_3$ in anhydrous DMSO. Then the perovskite precursor solution was spin-coated onto SnO_2 with a two-step program at 1000 and 6000 rpm for 5 and 27 s, respectively, in a nitrogen-filled glovebox. During the spin-coating process, different cases such as CB, DPS, DES, and DMS were dripped on the spinning substrate slowly for 5 s

before the end of the program, followed by annealing at 100 °C for 60 min. After cooling down to room temperature, the spiro-OMeTAD solution (73.2 mg in 1 mL CB) doped with 18 µL of Li-TFSI (520 mg/mL in ACN), 29 µL of FK209 Co (III) TFSI salt (300 mg/mL in ACN), and 29 µL tBP was coated at 4000 rpm for 30 s. Finally, 100 nm of gold was thermally evaporated under a pressure of 10^{-6} mbar as the back electrode.

For $FAPbI_3$, the fluorine-doped tin oxide (FTO) glasses were cleaned with detergent, deionized (DI) water, acetone and isopropanol using an ultrasonic bath for 20 min as a sequential process. The FTO substrates were treated by UV/ozone cleaner for 15 min before depositing the compact titanium dioxide (c-TiO_2). The c-TiO_2 film was deposited on the FTO substrates using spray pyrolysis method with 0.4 mL of acetylacetone, 0.6 mL of titanium diisopropoxide bis(acetylacetonate in 9mL of ethanol. This deposition process was implemented in-situ annealing for an hour on a 450 ℃ of a hotplate. The UV/ozone treatment was conducted for the FTO/c-TiO_2 substrates were cooled down for 15 min. The meso porous titanium dioxide (mp-TiO_2) solution was prepared as following the recipe that 150 mg of TiO_2 paste was diluted in 1 mL of ethanol solvent. The mp-TiO_2 film was implemented by spin coating method at 4000 rpm for 30 s. The mp-TiO_2 film deposited FTO/c-TiO_2 substrates were annealed to 450 ℃ at ambient air condition. The perovskite precursor was prepared 9 % of Pb excess with 1.25 M concentration in the stoichiometry of $FAPbI_3$ plus 40 mol% of Methylammonium Chloride in dimethylformamide (DMF): dimethyl sulfoxide (DMSO) with 8.5:1 of the volume ratio. Before deposition of the perovskite absorber layer, the FTO/c-TiO_2/mp-TiO_2 substrates were treated by UV/ozone cleaner for 15 min again. From perovskite film to spiro-MeOTAD layer were implemented in the glove box. The spin-coating program for the perovskite layer is a two-step spin coating method where the first step is 1000 rpm for 10 s and the second step is 5000 rpm for 20 s. During the second step of the spin-coating program, the coordinated solvent treatment was performed with CB and DMS one another. The FTO/c-TiO_2/mp-TiO_2/perovskite substrates were annealed for 10 min on the hotplate at 150 ℃. After finishing the produce of the perovskite film, n-octylammonium iodide (OAI) passivation layer was deposited that OAI solution is made up of 5mg of OAI in 1mL of isopropanol (IPA) with spin coating. The parameter is 4000 rpm for 30 s and the substrates were annealed for a short time at 100 ℃. The spiro-OMeTAD and gold layers were deposited by the same recipe as we used for $MAPbI_3$ devices.

Characterizations: For X-ray photoelectron spectroscopy (XPS) and Ultraviolet Photoelectron Spectroscopy (UPS), the perovskite layer prepared with various solvent treatments is analyzed with X-ray photoelectron spectroscopy using Al k-Alpha source (1486.5 eV) non-monochromitized X-ray. The photoelectrons are collected with the hemispherical analyzer from PHOIBOS HSA3500. The photo-emitted electrons are collected at a right angle to the surface of the sample. The detailed spectra of each element present on the samples are collected with a pass energy of 20 eV and a scan rate of 0.1 eV. The collected spectra were analyzed with the Casa XPS software, and the peaks were fitted with a mixed Gaussian-Lorentzian line shape with a Shirley background. The binding energy of the measured spectra is corrected with respect to the metallic Pb (137.00 eV) and advantageous carbon (285. 00 eV). FT-IR spectra were recorded from the neat powder of the respective analyte on a BRUKER JASCO FT-IR-4100 spectrometer. An Ocean Optics spectrometer (Flame) coupled with fiber optics was used to acquire transmission measurements with an integration time of about 0.15 s (spin-coating) to 0.4 s (annealing) per transmission spectrum and a wavelength spacing of about 1.3 nm in an N_2-filled glove box. The equation [$A_\lambda = -\log10(T_\lambda)$] was used to calculate the UV-Vis absorption spectra from the transmission spectra, where A_λ is the absorbance at a certain wavelength (λ), and T_λ is the corresponding transmitted radiation. The in-situ UV-Vis transmission/absorption measurements during spin-coating were performed using a setup. The in-situ UV-Vis transmission/absorption measurements during thermal annealing were performed using a custom-built heating stage with a hole that allows analog transmission. The in-situ PL measurements were carried out using a home-built setup in an N_2-filled glove box. Excitation was performed using a laser diode emitting at 405 nm and the PL emission was collected using an optical fiber coupled with an Ocean Optics spectrometer (Flame). A Jacobian correction was applied to the data transforming them from wavelength- to energy-space and fitting them using a Gaussian and a constant background. Integration times of 300 ms were used. The GIWAXS data were collected at the 12.3.2 microdiffraction beamline of the Advanced Light Source (ALS) in a custom-made analytical spin-coater allowing for simultaneous film-deposition and diffraction measurements. The SEM images were acquired in a Zeiss Crossbeam 550 system at low beam energies (5 kV 69 pA for the topview images and 2 kV 41 pA for the cross-sections). The cross-

section samples were mechanically cleaved with a glass-breaking tool. No conductive coatings were applied. For the steady-state PL, we used an Andor Kymera 193i spectrometer illuminated at 422 nm @ ~ 3 sun for 1 second. For the time-resolved photoluminescence (TRPL) we illuminated at 510 nm @ ~ 1 sun, with a stopping condition of 1e3 counts. The spectrometer was centered at either 760 or 770 nm with a bandwidth of 40 nm. It was run on a Lifespec 2, with a 5 nJ/cm^2 fluence. Nevertheless, PL and TRPL analysis was performed using Thot data management and analysis software.

Supporting Information

Supporting Information is available from the Wiley Online Library or from the author.

Acknowledgements

M. S. thanks the German Research Foundation (DFG) for funding (SPP2196, 431314977/GRK 2642). M. S. acknowledges funding by ProperPhotoMile. Project ProperPhotoMile is supported under the umbrella of SOLAR-ERA.NET Cofund 2 by The Spanish Ministry of Science and Education and the AEI under the project PCI2020-112185 and CDTI project number IDI-20210171; the Federal Ministry for Economic Affairs and Energy on the basis of a decision by the German Bundestag project number FKZ 03EE1070B and FKZ 03EE1070A and the Israel Ministry of Energy with project number 220-11-031. SOLAR-ERA.NET is supported by the European Commission within the EU Framework Programme for Research and Innovation HORIZON 2020 (Cofund ERA-NET Action, No. 786483). Furthermore, T.K. thanks the German Research Foundation (DFG) for funding (KO6414). This research used beamline 12.3.2, supported by Nobumichi Tamura, which is a resource of the Advanced Light Source, a U.S. DOE Office of Science User Facility under contract no. DE-AC02-05CH11231. In-situ characterizations at the Molecular Foundry were supported by the Office of Science, Office of Basic Energy Sciences, of the U.S. Department of Energy under Contract No. DE-AC02-05CH11231. The authors thank Simon Briesenick and Meredith Goudreau for their assistance in carrying out the in-situ characterization.

Received: ((will be filled in by the editorial staff))

Revised: ((will be filled in by the editorial staff))

Published online: ((will be filled in by the editorial staff))

Reference

[1] A. Kojima, K. Teshima, Y. Shirai, T. Miyasaka, *J. Am. Chem. Soc.* **2009**, 131, 6050-6051.

[2] J. Park, J. Kim, H.-S. Yun, M. J. Paik, E. Noh, H. J. Mun, M. G. Kim, T. J. Shin, S. il Seok, *Nature* **2023**, DOI 10.1038/s41586-023-05825-y.

[3] Z. Yao, W. Zhao, S. Liu, *J Mater Chem A Mater* **2021**, *9*, 11124.

[4] R. Jono, H. Segawa, *Chem Lett* **2019**, *48*, 877.

[5] S. Masi, A. F. Gualdrón-Reyes, I. Mora-Seró, *ACS Energy Lett* **2020**, *5*, 1974.

[6] M. Saliba, T. Matsui, J.-Y. Seo, K. Domanski, J.-P. Correa-Baena, M. Khaja, S. M. Zakeeruddin, W. Tress, A. Abate, A. Hagfeldt, M. Grä, *Cite this: Energy Environ. Sci* **2016**, *9*, 1989-1997.

[7] B. Conings, J. Drijkoningen, N. Gauquelin, A. Babayigit, A. Ethirajan, J. Verbeeck, J. Manca, E. Mosconi, F. de Angelis, H.-G. Boyen, B. Conings, J. Drijkoningen, A. Babayigit, A. Ethirajan, H. Boyen, N. Gauquelin, J. Verbeeck, E. Mosconi, F. de Angelis, Adv. Energy Mater. **2015**, 5, 1500477.

[8] N. J. Jeon, J. H. Noh, Y. C. Kim, W. S. Yang, S. Ryu, S. il Seok, *Nat Mater* **2014**, *13*, 897.

[9] Y.-J. Kang, S.-N. Kwon, S.-P. Cho, Y.-H. Seo, M.-J. Choi, S.-S. Kim, S.-I. Na, *ACS Energy Lett **2020***, 5, 2535-2545.

[10] Y. Wang, J. Wu, P. Zhang, D. Liu, T. Zhang, L. Ji, X. Gu, Z. David Chen, S. Li, *Nano Energy* **2017**, *39*, 616.

[11] A. D. Taylor, Q. Sun, K. P. Goetz, Q. An, T. Schramm, Y. Hofstetter, M. Litterst, F. Paulus, Y. Vaynzof, *Nat. commun.* **2021**, 12, 1878.

[12] D.-K. Lee, K.-S. Lim, J.-W. Lee, N.-G. Park, *J. Mater. Chem. A* **2021**, 9, 3018.

[13] S. Paek, P. Schouwink, E. N. Athanasopoulou, K. T. Cho, G. Grancini, Y. Lee, Y. Zhang, F. Stellacci, M. Khaja Nazeeruddin, P. Gao, *Chem. Mater.* **2017**, 29, 3490−3498.

[14] K. M. Lee, C. J. Lin, B. Y. Liou, S. M. Yu, C. C. Hsu, V. Suryanarayanan, M. C. Wu, *Solar Energy Materials and Solar Cells* **2017**, *172*, 368.

[15] T. Moot, A. R. Marshall, L. M. Wheeler, S. N. Habisreutinger, T. H. Schloemer, C. C. Boyd, D. R. Dikova, G. F. Pach, A. Hazarika, M. D. McGehee, H. J. Snaith, J. M. Luther, *Adv Energy Mater* **2020**, 10.

[16] E. J. Cassella, E. L. K. Spooner, J. A. Smith, T. Thornber, M. E. O'Kane, R. D. J. Oliver, T. E. Catley, S. Choudhary, C. J. Wood, D. B. Hammond, H. J. Snaith, D. G. Lidzey, *Adv. Energy Mater.* **2023***, 13,* 2203468.

[17] S. G. Kim, J. H. Kim, P. Ramming, Y. Zhong, K. Schötz, S. J. Kwon, S. Huettner, F. Panzer, N. G. Park, *Nat Commun* **2021**, *12*, 1554.

[18] V. Gutmann, *Coord Chem Rev* **1976**, *18*, 225.

[19] F. Arnaud-neu, R. Delgado, S. Chaves, *CRITICAL EVALUATION OF STABILITY CONSTANTS AND THERMODYNAMIC FUNCTIONS OF METAL COMPLEXES OF CROWN ETHERS (IUPAC Technical Report)*, Brazil, **2003**.
[20] J. C. Hamill, J. Schwartz, Y.-L. Loo, **2018**, *3*, 49.
[21] X. Huang, G. Deng, S. Zhan, F. Cao, F. Cheng, J. Yin, J. Li, B. Wu, N. Zheng, *ACS Cent Sci* **2022**, *8*, 1008.
[22] C. Fan Zheng, H. Takenaka, F. Wang, N. Z. Koocher, A. M. Rappe, *J. Phys. Chem. Lett* **2015**, *6*, 50.
[23] G. R. Berdiyorov, F. El-Mellouhi, M. E. Madjet, F. H. Alharbi, S. N. Rashkeev, Appl Phys Lett 2016, 108.
[24] G. R. Berdiyorov, F. El-Mellouhi, M. E. Madjet, F. H. Alharbi, F. M. Peeters, S. Kais, *Solar Energy Materials and Solar Cells* **2016**, *148*, 2.
[25] G. R. Berdiyorov, M. E. Madjet, F. El-Mellouhi, F. M. Peeters, *Solar Energy Materials and Solar Cells* **2016**, *148*, 60.
[26] F. Bella, G. Griffini, J. P. Correa-Baena, G. Saracco, M. Grätzel, A. Hagfeldt, S. Turri, C. Gerbaldi, *Science (1979)* **2016**, *354*, 203.
[27] H. Turren-Cruz, A. Hagfeldt, M. Saliba, *Science* **2018**, 362, 449–453.
[28] L. Shi, M. P. Bucknall, T. L. Young, M. Zhang, L. Hu, J. Bing, D. S. Lee, J. Kim, T. Wu, N. Takamure, D. R. McKenzie, S. Huang, M. A. Green, A. W. Y. Ho-Baillie, *Science (1979)* **2020**, *368*.
[29] P. Holzhey, P. Yadav, S. H. Turren-Cruz, A. Ummadisingu, M. Grätzel, A. Hagfeldt, M. Saliba, *Materials Today* **2019**, *29*, 10.
[30] N.-K. Kim, Y. H. Min, S. Noh, E. Cho, G. Jeong, M. Joo, S.-W. Ahn, J. S. Lee, S. Kim, K. Ihm, H. Ahn, Y. Kang, H.-S. Lee, D. Kim, *Scientific Reports* **2017**, 7, 4645.
[31] I. Barnes, K. H. Becker, I. Patroescu, *Atmos Environ* **1996**, *30*, 1805.
[32] A. A. Petrov, S. A. Fateev, V. N. Khrustalev, Y. Li, P. v Dorovatovskii, Y. v Zubavichus, E. A. Goodilin, A. B. Tarasov, *Chemistry of Materials* **2020**, *32*, 7739.
[33] S. Pratap, F. Babbe, N. S. Barchi, Z. Yuan, T. Luong, Z. Haber, T.-B. Song, J. L. Slack, C. v Stan, N. Tamura, C. M. Sutter-Fella, P. Müller-Buschbaum, *Nat Commun* **2021**, *12*, 5624.
[34] J. Li, A. Dobrovolsky, A. Merdasa, E. L. Unger, I. G. Scheblykin, *ACS Omega* **2018**, *3*, 14494.
[35] S. Kim, H. Oh, G. Kang, I. K. Han, I. Jeong, M. Park, *ACS Appl Energy Mater* **2020**, *3*, 6995.
[36] J. Li, X. Yuan, P. Jing, J. Li, M. Wei, J. Hua, J. Zhao, L. Tian, *RSC Adv.* **2016**, 6, 78311.
[37] N. G. Park, *Nat Sustain* **2021**, *4*, 192.
[38] R. Hanif, L. Qiao, S. J. Shiff, B. Rigas, *Journal of Laboratory and Clinical Medicine* **1997**, *130*, 576.
[39] T. H. Parliment, M. G. Kolor, I. Y. Maing, *IDENTIFICATION OF THE MAJOR VOLATILE COMPONENTS OF COOKED BEETS*, **n.d.**
[40] F. P. Byrne, S. Jin, G. Paggiola, T. H. M. Petchey, J. H. Clark, T. J. Farmer, A. J. Hunt, C. R. Mcelroy, J. Sherwood, *Sustain Chem Process* **2016**, *4*, 7.
[41] Y. Cui, S. Wang, L. Ding, F. Hao, *Advanced Energy and Sustainability Research* **2021**, *2*, 2000047.
[42] T. Bu, X. Liu, Y. Zhou, J. Yi, X. Huang, L. Luo, J. Xiao, Z. Ku, Y. Peng, F. Huang, Y.-B. Cheng, J. Zhong, *Energy Environ. Sci* **2017**, *10*, 2509.

[43] H. Beng Lee, M.-K. Jeon, N. Kumar, B. Tyagi, J.-W. Kang, H. B. Lee, M. Jeon, N. Kumar, B. Tyagi, J. Kang, *Adv. Funct. Mater.* **2019**, 29, 1903213.

[44] J. W. Lee, H. S. Kim, N. G. Park, *Acc Chem Res* **2016**, *49*, 311.

[45] H. Taherianfard, G. W. Kim, M. M. Byranvand, K. Choi, G. Kang, H. Choi, F. Tajabadi, N. Taghavinia, T. Park, *ACS Appl Energy Mater* **2020**, *3*, 1506.

[46] M. Yavari, M. Mazloum-Ardakani, S. Gholipour, M. Mahdi Tavakoli, S.-H. Turren-Cruz, N. Taghavinia, M. Grätzel, A. Hagfeldt, M. Saliba, G. M. Solvents Yavari, S. Turren-Cruz, A. Hagfeldt, M. Yavari, M. Mazloum-Ardakani, S. Gholipour, M. M. Tavakoli, M. Grätzel, A. San Claudio, S. Col San Manuel, M. Saliba, *Adv. Energy Mater* **2018**, *8*, 1800177.

[47] Q. Jiang, Y. Zhao, X. Zhang, X. Yang, Y. Chen, Z. Chu, Q. Ye, X. Li, Z. Yin, J. You, *Nat Photonics* **2019**, *13*, 460.

[48] J. Küffner, J. Hanisch, T. Wahl, J. Zillner, E. Ahlswede, M. Powalla, *ACS Appl Energy Mater* **2021**, *4*, 11700.

[49] J. Lee, M. Malekshahi Byranvand, G. Kang, S. Y. Son, S. Song, G.-W. Kim, T. Park, *J Am Chem Soc* **2017**, *139*, 12175.

[50] H. J. Snaith, A. Abate, J. M. Ball, G. E. Eperon, T. Leijtens, N. K. Noel, S. D. Stranks, J. Tse, W. Wang, K. Wojciechowski, W. Zhang, J. *Phys. Chem. Lett* **2014**, *5*.

(The table of contents entry should be 50–60 words long and should be written in the present tense. The text should be different from the abstract text.)

As a green solvent, DMSO has been widely used in the processing of perovskite to control its morphology and orientation. Unfortunately, the highly coordinating DMSO is not easily expelled from the thin films, which negatively affects the long-term stability of PSCs. Here, dimethyl sulfide (DMS) is introduced to revive perovskite by expelling DMSO from DMSO-intermediate phase compositions.

Weiwei Zuo,[1,†] Mahdi Malekshahi Byranvand,[1,2,†,*] Tim Kodalle,[3] Mohammadreza Zohdi,[1] Jaekeun Lim,[1] Brian Carlsen,[4] Theresa Magorian Friedlmeier,[5] Małgorzata Kot,[6] Chittaranjan Das,[1, 2] Jan Ingo Flege,[6] Wansheng Zong,[7] Antonio Abate,[8,9] Carolin M. Sutter-Fella,[3] Meng Li,[10] and Michael Saliba[1, 2,*]

Coordination Chemistry as a Universal Strategy for a Controlled Perovskite Crystallization

ToC figure ((Please choose one size: 55 mm broad × 50 mm high or 110 mm broad × 20 mm high. Please do not use any other dimensions))